JACS
JOURNAL OF THE AMERICAN CHEMICAL SOCIETY
Article
Cite This: J. Am. Chem. Soc. 2018, 140, 17624−17631
pubs.acs.org/JACS

Heterostructure-Promoted Oxygen Electrocatalysis Enables Rechargeable Zinc−Air Battery with Neutral Aqueous Electrolyte

Li An,[†,#] Zhiyong Zhang,[‡,#] Jianrui Feng,[§] Fan Lv,[§] Yuxuan Li,[†] Rui Wang,[†] Min Lu,[†] Ram B. Gupta,[⊥] Pinxian Xi,*[,†] and Sen Zhang*[,‡]

[†]State Key Laboratory of Applied Organic Chemistry, Key Laboratory of Nonferrous Metal Chemistry and Resources Utilization of Gansu Province, and College of Chemistry and Chemical Engineering, Lanzhou University, Lanzhou, 730000, People's Republic of China

[‡]Department of Chemistry, University of Virginia, Charlottesville, Virginia 22904, United States

[§]Department of Materials Science & Engineering, College of Engineering, Peking University, Beijing 100871, People's Republic of China

[⊥]Department of Chemical & Life Science Engineering, College of Engineering, Virginia Commonwealth University, Richmond, Virginia 23284, United States

Supporting Information

ABSTRACT: Neutral aqueous zinc−air batteries (ZABs) are an emerging type of energy devices with substantially elongated lifetime and improved recyclability compared to conventional alkaline ZABs. However, their development is impeded by the lack of robust bifunctional catalyst at the air-electrode for the oxygen evolution reaction (OER) and the oxygen reduction reaction (ORR). Here, we report the controlled synthesis of $NiFe_2O_4/FeNi_2S_4$ heterostructured nanosheets (HNSs) that are highly efficient in catalyzing OER and ORR, therefore enabling neutral rechargeable ZABs. Associated with the formation of abundant oxide/sulfide interfaces over $NiFe_2O_4/FeNi_2S_4$ HNSs' surfaces, the catalyst's oxygen binding energy can be effectively tuned to enhance the OER and ORR activities, as revealed by the density functional theory calculations. In 0.2 M phosphate buffer solution, the optimized $NiFe_2O_4/FeNi_2S_4$ HNSs present an excellent oxygen electrocatalytic activity and stability, with much lower OER and ORR overpotentials than single-component $FeNi_2S_4$ or $NiFe_2O_4$ and with negligible performance decay in accelerated durability testing. When used as an air-electrode, the $NiFe_2O_4/FeNi_2S_4$ HNSs can deliver a power density of 44.4 mW cm^{-2} and a superior cycling stability (only 0.6% decay after 900 cycles at 0.5 mA cm^{-2}), making the resultant ZAB the most efficient and robust one with a neutral aqueous electrolyte reported to date. This work highlights the essential function of the heterostructure interface in oxygen electrocatalysis, opening a new avenue to advanced neutral metal−air batteries.

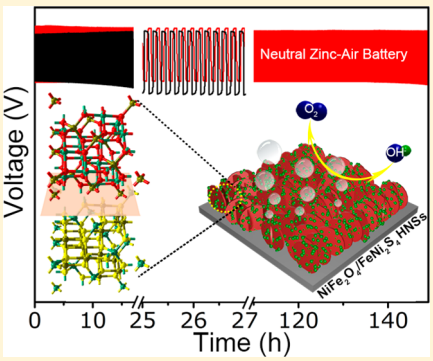

1. INTRODUCTION

Developing efficient energy storage and conversion devices with low environmental impact is central to our ability to secure society's energy and environmental sustainability.[1−3] Due to their high theoretical energy density and low cost, zinc−air batteries (ZABs) are considered to be one of the most promising candidates to fulfill our demands for future power devices.[4−6] Conventional ZABs use alkaline electrolytes and are restricted by high causticity and fast carbonation of electrolytes as well as zinc dendrite formation during charge and discharge cycles.[7,8] The alkaline electrolyte carbonation leads to a decrease in ionic conductivity, while zinc dendrites cause short circuiting of the device;[9] both are detrimental to the lifetime and recyclability of ZABs. Using neutral-pH electrolytes, the ZABs follow the same electrochemical reactions as in alkaline ones (air-cathode: $O_2 + 2H_2O + 4e^- \rightleftharpoons 4OH^-$; zinc anode: $Zn + 2OH^- \rightleftharpoons ZnO + H_2O + 2e^-$),[10] while working in more environment-friendly and less corrosive conditions, which can potentially mitigate the carbonation and dendrite issues as well as make ZABs rechargeable.[11] However, the neutral media normally possess lower ionic conductivity and extremely low OH^- concentration. As a result, the key electrochemical reactions at the air-cathode of ZABs, the oxygen evolution reaction (OER) during charge and the oxygen reduction reaction (ORR) during discharge, are prone to be kinetically more sluggish in neutral media.[12,13] Breakthroughs in highly active and durable bifunctional catalysts that operate optimally in a neutral environment for both OER and ORR are therefore urgently needed to maximize the neutral ZABs' performance. Although precious metals Pt, Ir, and Ru and their oxides are commonly studied catalysts,[14−16] electrocatalysts based on earth abundant elements are much more

Received: September 10, 2018
Published: November 7, 2018

DOI: 10.1021/jacs.8b09805
J. Am. Chem. Soc. 2018, 140, 17624−17631

desirable and have yet to be achieved for viable applications of rechargeable ZABs (RZABs).

In this article, we present a controlled sulfidation approach to $NiFe_2O_4/FeNi_2S_4$ heterostructured nanosheets (HNSs) that can efficiently catalyze OER and ORR to enable neutral RZABs. Recent studies have indicated that Fe-based and Ni-based nanomaterials are promising nonprecious metal catalysts for oxygen electrochemistry.[17−20] For example, Ni−Fe mixed oxide/hydroxide and their derivatives perform OER at a benchmark activity of 10 mA cm^{-2} with encouraging low overpotentials (~0.3−0.5 V),[21−23] while spinel-structured Ni−Fe mixed oxides have been reported to exhibit ORR activities comparable to Pt.[24] Despite that these achievements were observed in alkaline conditions, we envision that further tuning of Ni−Fe mixed oxide-based nanomaterials should allow appealing OER and ORR performances to be reached in neutral electrolytes.[25,26] On the other hand, engineering rational heterostructures within catalysts has been deemed as an important strategy to enhance the catalytic properties via interfacial electronic coupling.[27−29] Such an effect has been demonstrated in Au-M_xO_y (M = Ni, Co, Fe, and CoFe) core−shell nanoparticles wherein precious metal Au can substantially improve M_xO_y's OER kinetics.[30] Herein, we report this heterostructure-induced interfacial effect can be manipulated in completely nonprecious $NiFe_2O_4/FeNi_2S_4$ HNSs. By creating oxide/sulfide interfaces over $FeNi_2S_4$ nanoparticle-modified $NiFe_2O_4$ NS surfaces, catalyst surface binding energy with oxygenated species can be improved to accelerate the kinetics for both OER and ORR, as indicated by density functional theory (DFT) calculations. The bifunctional catalytic properties can be optimized by synthetically tuning the oxide/sulfide interface intensities and profiles, allowing our $NiFe_2O_4/FeNi_2S_4$ HNSs to exhibit much higher OER and ORR activity in a 0.2 M phosphate buffer solution at pH = 7.0 than pristine $NiFe_2O_4$ and $FeNi_2S_4$. Moreover, the RZABs based on the optimized $NiFe_2O_4/FeNi_2S_4$ HNSs and neutral electrolyte are constructed and can deliver a power density of 44.4 mW cm^2 and a negligible decay after 900-cycle stability testing, making them the most robust RZABs in neutral conditions reported to date.

2. EXPERIMENTAL SECTION

2.1. Materials. $Ni(NO_3)_2·6H_2O$ (98.0%), $Fe(NO_3)_3·9H_2O$ (99.0%), urea (99.0%), NH_4F (99.0%), KOH (99.0%), $Na_2S·9H_2O$, and Nafion (5 wt %) were purchased from Aladdin. The deionized water was obtained from a Millipore Autopure system (18.2 MΩ, Millipore Ltd., USA). The commercial carbon fiber paper (CFP) was purchased from Fuel Cell Store. All other materials for electrochemical measurements were of analytical grade and used without further purification.

2.2. Synthesis of $NiFe_2O_4$ NSs, $NiFe_2O_4/FeNi_2S_4$ HNSs, and $FeNi_2S_4$ NSs. Typically, 207 mg of $Ni(NO_3)_2·6H_2O$ and 577 mg of $Fe(NO_3)_3·9H_2O$ were first dissolved in 40 mL of deionized water. Then 216 mg of urea and 135 mg of NH_4F were slowly added into the solution under stirring. After an additional 10 min of stirring, the above solution was transferred into a 50 mL Teflon-lined stainless steel autoclave, with two pieces of CFP (3 × 4 cm^2) immersed vertically. The autoclave was sealed and heated at 120 °C for 12 h and then cooled to room temperature naturally. After being rinsed with deionized water and ethanol several times, the CFP was dried at 80 °C overnight and then annealed at 300 °C in air for 2 h to produce $NiFe_2O_4$ NSs. The $NiFe_2O_4/FeNi_2S_4$ HNSs were obtained by heating the $NiFe_2O_4$ NSs with 100 mg of $Na_2S·9H_2O$ in 40 mL of DI water at 100 °C for a desired duration ($NiFe_2O_4/FeNi_2S_4$ HNSs, 1 h; $NiFe_2O_4/FeNi_2S_4$ HNSs, 3 h; $NiFe_2O_4/FeNi_2S_4$ HNSs, 6 h; and $NiFe_2O_4/FeNi_2S_4$ HNSs, 9 h). For simplicity, $NiFe_2O_4/FeNi_2S_4$ HNSs are used to represent $NiFe_2O_4/FeNi_2S_4$ HNSs-3 h in this work unless otherwise mentioned. Extending the sulfidation duration to 12 h will yield the total vulcanized product of $FeNi_2S_4$ NSs.

2.3. Physical Characterizations. Powder X-ray diffraction (XRD) patterns were collected on a Rigaku D/Max-2400 diffractometer with Cu Kα radiation (λ = 1.541 78 Å). The morphology of the products was analyzed by field emission scanning electron microscopy (FE-SEM, FEI Sirion-200 SEM) at an acceleration voltage of 5 kV. Transmission electron microscopy (TEM) and high-resolution transmission electron microscopy (HRTEM) images were collected on a Tecnai G2 F30 field emission transmission electron microscope. X-ray photoelectron spectroscopy (XPS) was carried out on a Phi X-tool instrument with Mg Kα ($h\nu$ = 1253.6 eV) as the excitation source. The binding energies obtained in the XPS spectral analysis were corrected for specimen charging by referencing C 1s to 284.6 eV. Elemental mappings were performed on the same TFM-EDS microscope. Inductively coupled plasma optical emission spectrometry (ICP-OES) analyses were performed on a Plasma Quant PQ9000 ICP spectrometer.

2.4. Electrochemical Analyses. All electrochemical investigations were performed at room temperature on a CHI 760e electrochemical workstation (CHI Instruments, Shanghai Chenhua Instrument Corporation, China) using a conventional three-electrode setup, with a Ag/AgCl (saturated KCl) reference electrode and a Pt wire counter electrode, while the working electrode (WE) was either the CFP-supported $NiFe_2O_4/FeNi_2S_4$ HNSs, $FeNi_2S_4$ NSs, or $NiFe_2O_4$ NSs (geometric area = 1 cm^2) or a rotating ring-disk electrode (RRDE) with a Pt ring and a glass carbon disk. An O_2-saturated 0.2 M phosphate buffer solution (PBS, pH = 7.0, room temperature) was employed as the electrolyte to evaluate the electrocatalytic performances of both OER and ORR. All potentials were reported vs a reversible hydrogen electrode (RHE), according to the Nernst equation ($E_{RHE} = E_{Ag/AgCl} + 0.0591 \times pH + 0.197$). It needs to be noted that all the linear sweep voltammetry (LSV) curves were reported with iR correction and vs an RHE.

To fabricate the RRDE electrode, the as-synthesized catalyst was carefully scraped off from CFP. A 3 mg amount of the catalyst was dispersed in a solvent consisting of 1470 μL of dimethylformamide (DMF) and 30 μL of Nafion under sonication to form a uniform ink. A 12.6 μL amount of the catalyst ink was drop-cast on the RRDE and dried under vacuum to achieve a loading of 0.2 mg cm^{-2}. In order to determine the reaction pathway of OER, the ring potential was held constant at 1.5 V (vs RHE) to oxidize intermediates in O_2-saturated 0.2 M PBS. Besides, to ensure that the oxidation current originates from oxygen evolution rather than other side reactions and to calculate the Faradaic efficiency (FE) of the system, the ring potential of the RRDE was held constant at 0.40 V vs RHE to reduce the O_2 formed from the catalyst coated on the RRDE in N_2-saturated 0.2 M PBS. The FE is calculated as follows:

$$\mathrm{FE} = I_r/(I_d N)$$

where I_d denotes the disk current, I_r denotes the ring current, and N denotes the current collection efficiency of the RRDE, which was determined to be 0.2.[31,32]

The relationship between the measured currents (j) with various electrode rotating speeds (ω) under fixed potentials can be expressed according to the Koutechky−Levich (K-L) equation as follows:[33]

$$\frac{1}{j} = \frac{1}{j_k} + \frac{1}{B\omega^{1/2}}$$

where j_k is the kinetic current and ω is the electrode rotating rate. B is obtained from the slope of the K-L plots based on the Levich equation below:

$$B = 0.2nF(D_{O_2})^{2/3}\nu^{-1/6}C_{O_2}$$

where n represents the transferred electron number per oxygen molecule. F is the Faraday constant (F = 96485.3 C mol^{-1}). D_{O_2} is the

DOI: 10.1021/jacs.8b09805
J. Am. Chem. Soc. 2018, 140, 17624−17631

diffusion coefficient of O_2 in the electrolyte (D_{O_2} = 1.9 × 10^{-5} cm^2 s^{-1}). ν is the kinetic viscosity (ν = 0.01 cm^2 s^{-1}). C_{O_2} is the bulk concentration of C_{O_2} = 1.2 × 10^{-6} mol cm^{-3}). The constant 0.2 is adopted when the rotation speed is expressed in rpm.

2.5. Fabrication of RZAB. The alkaline zinc−air batteries were assembled with a Zn plate as the anode, as-synthesized catalysts as the air-cathode, and 6.0 M KOH as the electrolyte. The polarization and galvanostatic discharge measurements were performed by LSV (5 mV s^{-1}) and chronopotentiometric response (CP), respectively, using a CHI 760E electrochemical work station. The galvanostatic charge and discharge were performed at room temperature by a LAND testing system at 10 min per cycle. The neutral zinc−air battery was investigated using the same setup, while 4.0 M NH_4Cl + 2.0 M KCl was used as the electrolyte. $NH_3{\cdot}H_2O$ was used to adjust the pH of this solution to 7.0. The round-trip overpotential is calculated based on the following equation: voltage overpotential = E_{cha} - E_{dis}. Voltage efficiency is determined by round-trip efficiency = $\frac{E_{dis}}{E_{cha}}$, where E_{cha} and E_{dis} represent the potentials at the end of charge and discharge profiles of each cycle.

2.6. Theoretical Calculations. The DFT calculations were carried out using the Vienna ab Initio simulation package (VASP) with the projector augmented wave (PAW) pseudopotentials[34] and the function of Perdew, Burke, and Ernzerhof (PBE)[35] based on the generalized gradient approximation (GGA). A cutoff energy of 400 eV was used for the plane-wave basis set. The Brillouin zone was sampled on the basis of the Monkhorst−Pack scheme[36] with a 3 × 3 × 1 k-point mesh. The convergence criteria of the self-consistent field (SCF) for electronic relaxation and force for atomic relaxation were 1 × 10^{-5} eV and 0.02 eV $Å^{-1}$, respectively. The surface energy (γ) is defined by $\gamma = (E_{slab} - nE_{bulk})/2A$, where E_{slab} is the total energy of the slab, E_{bulk} is the total energy of the bulk per unit cell, n is the number of bulk unit cells contained in the slab, and A is the exposed area of one side of the slab. The oxygen adsorption energy E_O was defined as $E_O = E_{sub+a} - E_{sub} - E_a$, where E_{sub+a}, E_{sub}, and E_a are the total energies of catalyst substrates with the oxygen adsorbate, clean substrates, and the isolated oxygen atom, respectively. Spin polarizations were considered in all the calculations.

3. RESULTS AND DISCUSSION

The $NiFe_2O_4/FeNi_2S_4$ HNSs are synthesized by a wet-chemical sulfidation method, as illustrated in Scheme 1. The

Scheme 1

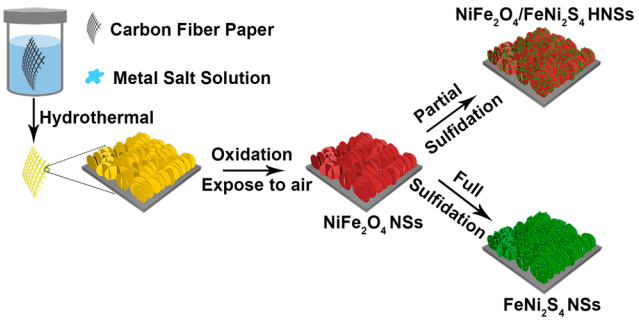

$NiFe_2O_4$ NSs are first prepared by a hydrothermal treatment of CFP in the presence of Fe and Ni salt solution and a subsequent calcination in air at 300 °C for 2 h (Experimental Section). The as-obtained $NiFe_2O_4$ NSs are then aged in Na_2S solution to allow $FeNi_2S_4$ nanoparticles to be formed over the $NiFe_2O_4$ NS surface. During this process, the surface oxygen anions of $NiFe_2O_4$ are exchanged with S^{2-}, yielding $FeNi_2S_4$ nanoscale domains. We notice that the $FeNi_2S_4$ nanoparticle density is increased with the reaction time, while a 12 h sulfidation can fully convert $NiFe_2O_4$ to $FeNi_2S_4$. We prepared a series of $NiFe_2O_4/FeNi_2S_4$ HNSs with different reaction times for a systematic study of the heterostructure interface effect in electrocatalysis. The Fe/Ni molar ratios of these samples were analyzed by ICP-OES (Table S1). We find that the Fe/Ni molar ratios of $NiFe_2O_4$ NSs and $FeNi_2S_4$ NSs are 2.08:1 and 1:1.91, respectively, while that of $NiFe_2O_4/FeNi_2S_4$ HNSs-1 h, -3 h, -6 h, and -9 h monotonously decreases with the sulfidation reaction time. These results indicate that a part of Fe is gradually dissolved during the phase transformation from $NiFe_2O_4$ to $FeNi_2S_4$, probably due to the favorable thermodynamic stability of $FeNi_2S_4$ (known as a *violarite*) under our sulfidation condition.

The SEM images in Figures 1A and S1 show that the as-synthesized $NiFe_2O_4$ are composed of NSs with a lateral size of

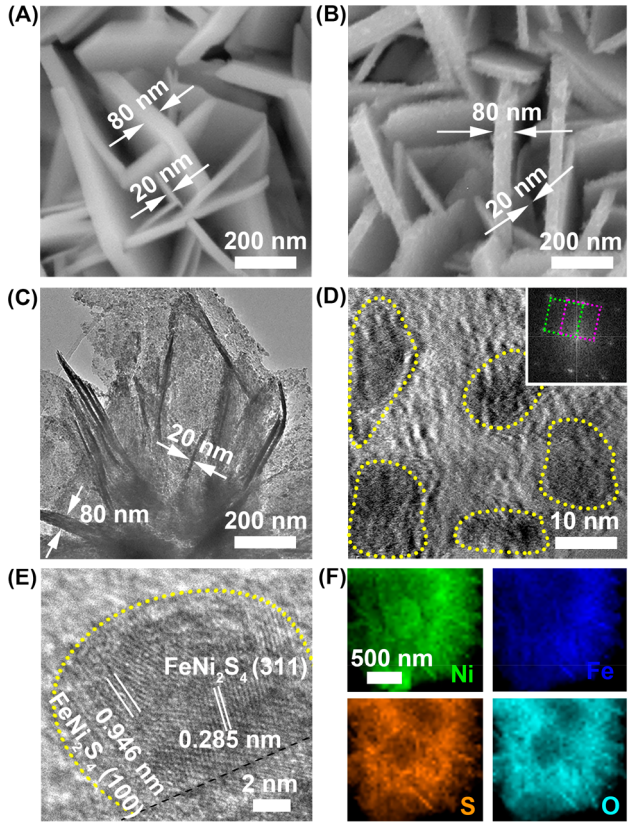

Figure 1. (A, B) SEM images of (A) $NiFe_2O_4$ NSs and (B) $NiFe_2O_4/FeNi_2S_4$ HNSs. (C, D) TEM (C) and HRTEM (D) images of $NiFe_2O_4/FeNi_2S_4$ HNSs. Inset of (D) displays the corresponding FFT pattern. (E) HRTEM image showing representative interface profiles within $NiFe_2O_4/FeNi_2S_4$ HNSs. (F) TEM-EDS elemental mapping images of $NiFe_2O_4/FeNi_2S_4$ HNSs.

several micrometers and a thickness of 20−80 nm. After the sulfidation, $NiFe_2O_4/FeNi_2S_4$ inherit the NSs' size and morphology with the $FeNi_2S_4$ nanodomains uniformly distributed on the surface of $NiFe_2O_4$ NSs, roughening the NSs' surface, as clearly seen in the SEM (Figure 1B) and TEM images (Figures 1C and S2). The roughened surface is also observed in the $FeNi_2S_4$ sample even after a full sulfidation (Figures S1C and S2C).

HRTEM was used to reveal the structure details and change in the course of our controlled sulfidation. The as-synthesized $NiFe_2O_4$ NSs are a single crystal for each individual sheet (Figure S3), with the (100) facet exposed in the basal surface,

DOI: 10.1021/jacs.8b09805
J. Am. Chem. Soc. 2018, 140, 17624−17631

as indicated in HRTEM images and a lattice fringe viewed parallel to the basal plane in Figure S4. After a 3 h sulfidation, it is clearly seen that abundant particles around 10−20 nm (highlighted by a yellow dashed line) are formed in the surface of NSs and are surrounded by a low-contrast $NiFe_2O_4$ matrix, suggesting the successful construction of $NiFe_2O_4/FeNi_2S_4$ heterostructure interfaces (Figure 1D). Meanwhile, controlling sulfidation time from 1 to 9 h can readily increase the density of the heterointerfaces over our samples (Figure S5). The corresponding fast Fourier transform (FFT) pattern based on the HRTEM image also confirms the formation of a mixed cubic phase of $NiFe_2O_4$ (purple) and $FeNi_2S_4$ (green) in the product (Figure 1D, inset).

It is noteworthy that such a nanoparticles-over-NSs architecture determines the variety of interface profiles within $NiFe_2O_4/FeNi_2S_4$ HNSs, as the curving boundary between $NiFe_2O_4$ and $FeNi_2S_4$ allows both low-index and high-index facets from each component to be possibly attached (Figures 1E and S6). For example, we find lattice fringes that well match the (100) and (311) planes of $NiFe_2O_4$ and $FeNi_2S_4$, respectively. In addition, since $FeNi_2S_4$ nanoparticles are well dispersed over NSs, the large-scale TEM-energy-dispersive X-ray spectroscopy (EDS, Figure S7) and TEM-EDS elemental mapping (Figure 1F) demonstrate that Ni, Fe, O, and S are uniformly distributed in the heterostructured product. In addition, the XRD patterns of $NiFe_2O_4/FeNi_2S_4$ HNSs, $NiFe_2O_4$ NSs, and $FeNi_2S_4$ NSs are shown in Figure 2A.

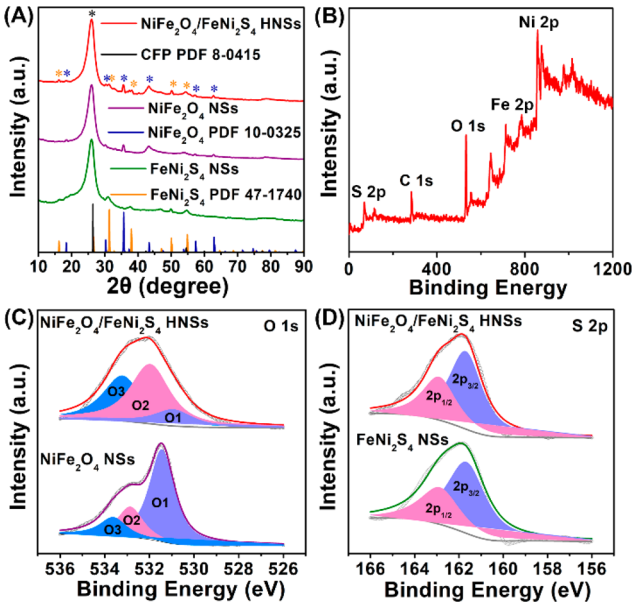

Figure 2. (A) XRD patterns of $NiFe_2O_4/FeNi_2S_4$ HNSs, $NiFe_2O_4$ NSs, and $FeNi_2S_4$ NSs. (B) XPS survey spectrum of $NiFe_2O_4/FeNi_2S_4$ HNSs. (C, D) High-resolution XPS spectra of (C) O 1s in $NiFe_2O_4/FeNi_2S_4$ HNSs and $NiFe_2O_4$ NSs and (D) S 2p in $NiFe_2O_4/FeNi_2S_4$ HNSs and $FeNi_2S_4$ NSs.

The diffraction peaks of $NiFe_2O_4/FeNi_2S_4$ HNSs confirm the presence of both cubic *trevorite* $NiFe_2O_4$ (PDF Card No. 10-0325; $a = b = c = 8.339$ Å) and cubic *violarite* $FeNi_2S_4$ (PDF Card No. 47-1740; $a = b = c = 9.458$ Å) with the same space group of *Fd*3*m* (Figure S8), in line with the aforementioned HRTEM results.

XPS was also conducted to investigate the electronic states of elements over our samples (Figure 2B). As shown in Figure S9, both the Ni 2p and Fe 2p high-resolution XPS spectra of $NiFe_2O_4/FeNi_2S_4$ HNSs are best fitted with double spin−orbit doublets (2+, 3+) and two shakeup satellites.[37,38] The relative intensity of Ni^{2+}/Ni^{3+} for $NiFe_2O_4/FeNi_2S_4$ HNSs after a 3 h sulfidation (1.45:1) is lower than that of pristine $NiFe_2O_4$ NSs (2.13:1) while higher than $FeNi_2S_4$ NSs (0.83:1) (Table S2). Meanwhile, the majority of Fe in the surface of $NiFe_2O_4/FeNi_2S_4$ HNSs exists in the +3 oxidation state. The atomic ratio of Fe^{2+}/Fe^{3+} for $NiFe_2O_4/FeNi_2S_4$ HNSs (1:1.18) also falls in the middle of $NiFe_2O_4$ NSs (1:1.87) and $FeNi_2S_4$ NSs (1:0.60) (Table S3), suggesting the strong cation interactions after the formation of $NiFe_2O_4/FeNi_2S_4$ interfaces.[39,40] More interesting, the peaks of O1, O2, and O3 in Figure 2B appear at 531.44, 532.85, and 533.62 eV for pristine $NiFe_2O_4$ NSs and then negatively shift to 530.93, 531.97, and 533.21 eV for $NiFe_2O_4/FeNi_2S_4$ HNSs, respectively (Figure 2C). Correspondingly, the electron binding energies of S $2p_{1/2}$ and S $2p_{3/2}$ have a positive shift of about 0.04 eV after the formation of $NiFe_2O_4/FeNi_2S_4$ HNSs (Figure 2D), confirming the charge transfer from S to O. The cation interaction and charge transfer are anticipated to play an important role in tuning the electronic structure of metal centers in $NiFe_2O_4/FeNi_2S_4$ interfaces and thus influencing the OER/ORR electrocatalysis kinetics.

To further understand the interface−catalysis correlation, we constructed two $NiFe_2O_4/FeNi_2S_4$ heterostructure models with $NiFe_2O_4$ and $FeNi_2S_4$ clusters attached through their (311) or (100) planes (to represent high-index interface and low-index interface, denoted as $NiFe_2O_4/FeNi_2S_4$-(311) and $NiFe_2O_4/FeNi_2S_4$-(100)) and implemented the DFT calculations (Figure 3A and B) to evaluate their surface energetics. Differential charge density of the interfacial model (Figure 3C) shows that oxygen prefers to adsorb on surface Ni at the

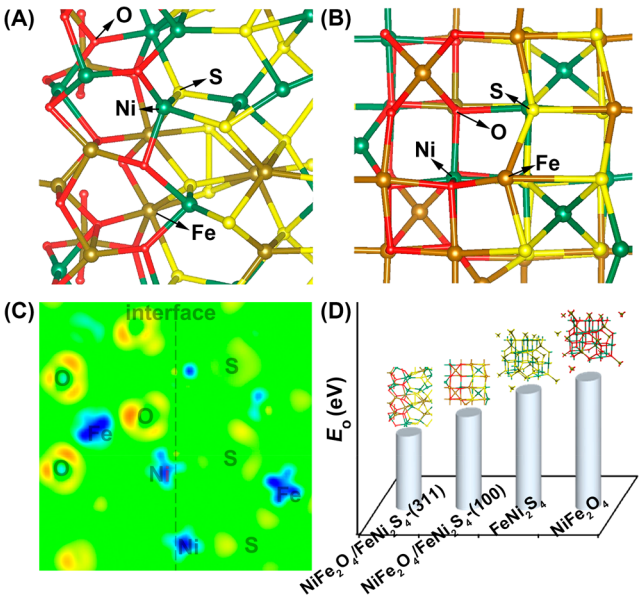

Figure 3. (A, B) Optimized geometry of oxygen adsorption over the $NiFe_2O_4/FeNi_2S_4$ (311) interface model (A) and the $NiFe_2O_4/FeNi_2S_4$ (100) interface model (B). (C) Differential charge density of the cross-sectional view of the $NiFe_2O_4/FeNi_2S_4$ (311) interface model. The red/light (blue/dark) areas mark an increase (decrease) of the electron density. (D) Computational surface E_O comparison of $NiFe_2O_4/FeNi_2S_4$-(311), $NiFe_2O_4/FeNi_2S_4$-(100), $FeNi_2S_4$, and $NiFe_2O_4$.

DOI: 10.1021/jacs.8b09805
J. Am. Chem. Soc. 2018, 140, 17624−17631

interface and indicates that the electron is transferred from $FeNi_2S_4$ to the $NiFe_2O_4$ domain, driven by the higher electronic affinity of O. These further imply the strong electronic interaction between $NiFe_2O_4$ and $FeNi_2S_4$ domains. Previously, Nørskov et al. performed a series of theoretical calculations on the ORR and OER kinetics based on metals[41] and metal oxide[42] catalysts. Their calculations demonstrated linear scaling relations between *O, *OH, and *OOH intermediates, which allows the use of oxygen adsorption energy (E_O) as a general descriptor to predict/evaluate the ORR and OER activities.[43,44] The calculated E_O follows the order $NiFe_2O_4/FeNi_2S_4$-(311) (2.91 eV) < $NiFe_2O_4/FeNi_2S_4$-(100) (3.68 eV) < $FeNi_2S_4$ (4.60 eV) < $NiFe_2O_4$ (5.09 eV) (Figure 3D and Table S4), clearly demonstrating that interfaces can effectively decrease E_O regardless of interface profiles ($NiFe_2O_4/FeNi_2S_4$-(311) or $NiFe_2O_4/FeNi_2S_4$-(100)). It is widely known that metal oxide catalysts are subject to an overstrong oxygen adsorption, which makes reaction kinetics sluggish.[45−48] Therefore, the substantially decreased E_O at the $NiFe_2O_4/FeNi_2S_4$ interface is crucial for enhancing our catalysts' oxygen electrocatalytic properties.

The $NiFe_2O_4/FeNi_2S_4$ HNSs grown on CFP were directly used as working electrodes in O_2-saturated 0.2 M PBS (pH = 7.0) to assess their electrocatalytic performance toward OER. As illustrated in Figure 4A, the $NiFe_2O_4/FeNi_2S_4$ HNSs show

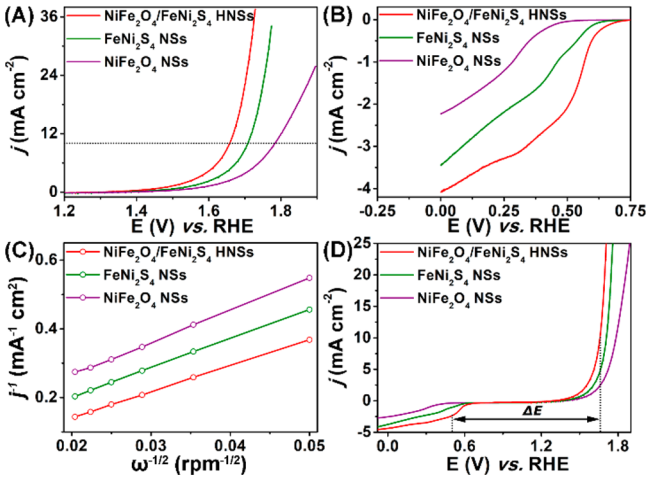

Figure 4. (A, B) OER (A) and ORR (B) polarization curves of $NiFe_2O_4/FeNi_2S_4$ HNSs, $FeNi_2S_4$ NSs, and $NiFe_2O_4$ NSs in O_2-saturated PBS. (C) Koutechy−Levich plots of all catalysts for ORR. (D) LSV curves of $NiFe_2O_4/FeNi_2S_4$ HNSs, $FeNi_2S_4$ NSs, and $NiFe_2O_4$ NSs for both OER and ORR measurements. (scan rate: 2 mV s^{-1}, rotation speed: 1600 rpm, catalyst loading: 0.3 mg cm^{-2}, normalized to the surface area of a 3 mm diameter GC electrode).

an overpotential (η) of 253 mV at a current density of 1 mA cm^{-2}, which is the best among catalysts for OER in this condition reported to date (Table S5). To reach the current density of 10 mA cm^{-2}, $NiFe_2O_4/FeNi_2S_4$ HNSs require an η of 429 mV, superior to $FeNi_2S_4$ NSs (478 mV) and $NiFe_2O_4$ NSs (553 mV). Figure S10 displays the corresponding rotating ring disk electrode results. Due to the almost negligible ring current, the OER process occurring on the $NiFe_2O_4/FeNi_2S_4$ HNSs is dominated by the four-electron pathway $4OH^- \rightarrow O_2 + 2H_2O + 4e^-$. Furthermore, the OER FE is measured to be around 99.0% on $NiFe_2O_4/FeNi_2S_4$ HNSs, which confirms that the observed oxidation current is almost fully attributed to water oxidation.[32,49]

On the other hand, $NiFe_2O_4/FeNi_2S_4$ HNSs obtained after a 3 h sulfidation present a clear oxygen reduction peak and current in the CV plot in O_2-saturated PBS, while no apparent signal is observed in a N_2 atmosphere (Figure S11). The onset potential for ORR is 0.715 V on $NiFe_2O_4/FeNi_2S_4$ HNSs, which is more positive than those on $FeNi_2S_4$ NSs (0.648 V) and $NiFe_2O_4$ NSs (0.503 V) (Figure 4B). Remarkably, $NiFe_2O_4/FeNi_2S_4$ HNSs exhibit a half-wave potential ($E_{1/2}$) at 0.507 V, confirming their much higher activity than $FeNi_2S_4$ NSs ($E_{1/2}$ at 0.361 V) and $NiFe_2O_4$ NSs ($E_{1/2}$ at 0.273 V) (Figure S12). Figure 4C shows the K-L plots on different catalysts, derived from their relevant ORR linear polarization curves (LSVs) (Figure S13). The calculated number of transferred electrons (n) on $NiFe_2O_4/FeNi_2S_4$ HNSs, $FeNi_2S_4$ NSs, and $NiFe_2O_4$ NSs in 0.2 M PBS are 3.70, 3.62, and 2.91, respectively, indicating a quasi-four-electron process for ORR occurring on $NiFe_2O_4/FeNi_2S_4$ HNSs.[50]

The $NiFe_2O_4/FeNi_2S_4$ HNSs with different sulfidation times were also carefully investigated to identify the optimal heterostructured catalyst. As clearly seen in Figure S14, a 3 h sulfidation can endow the catalyst with much lower overpotentials for both OER and ORR than 1, 6, or 9 h treatments. It is possibly because $NiFe_2O_4/FeNi_2S_4$ HNSs obtained after a 3 h sulfidation possess a suitable heterointerface density and a more favorable interface profile than from 1, 6, or 9 h treatment. According to our DFT calculation, different interfacial configurations can significantly vary E_O. Specifically, a high-index (311) interface can lead to a much lower E_O (2.91 eV) compared with a (100) interface (3.68 eV). We theorize that a 3 h sulfidation might equip $NiFe_2O_4/FeNi_2S_4$ HNSs with a more desirable interface configuration. Based on the best sulfidation condition (3 h), as summarized in Figure 4D and Table S6, the $NiFe_2O_4/FeNi_2S_4$ HNSs-3 h have an excellent bifunctional activity for both OER and ORR in neutral electrolyte, with a much improved ΔE of 1.152 V ($\Delta E = E_{j=10} - E_{1/2}$) compared with $FeNi_2S_4$ HNSs (1.347 V) and $NiFe_2O_4$ NSs (1.510 V).[32]

Our $NiFe_2O_4/FeNi_2S_4$ HNSs also exhibit an excellent stability for OER and ORR. As shown in Figure S15A, the $NiFe_2O_4/FeNi_2S_4$ HNSs display almost no decay of ORR activity after 5000 CV cycles through an accelerated durability test (ADT). Meanwhile, only a slight $E_{j=10}$ attenuation of 7 mV was observed after the ADT testing for OER, confirming $NiFe_2O_4/FeNi_2S_4$ HNSs' high stability for OER (Figure S15B). After the ADT test, there is no obvious change in the structure and morphology of $NiFe_2O_4/FeNi_2S_4$ HNSs, as evident from the XRD patterns and TEM images in Figure S16.

With the excellent bifunctional oxygen electrocatalytic property, $NiFe_2O_4/FeNi_2S_4$ HNSs can serve as the air-electrode to enable high-performance RZABs. To demonstrate the advantage of using a neutral electrolyte, we first constructed a ZAB with 6 M KOH as the electrolyte.[51] This alkaline ZAB shows a high open-circuit voltage (OCV) of 1.49 V and a high peak power density of 187 mW cm^{-2} (Figure S17), outperforming the state-of-the-art ZABs (Table S7). However, as expected for an alkaline ZAB, the cell voltage overpotential rapidly increases from 0.89 V to 1.24 V after 190 cycles, and the corresponding round-trip efficiency decreases from 55.8% to 39.2% (Figure 5A and B). The stability of RZAB with $NiFe_2O_4/FeNi_2S_4$ HNSs as the air-electrode is

DOI: 10.1021/jacs.8b09805
J. Am. Chem. Soc. 2018, 140, 17624−17631

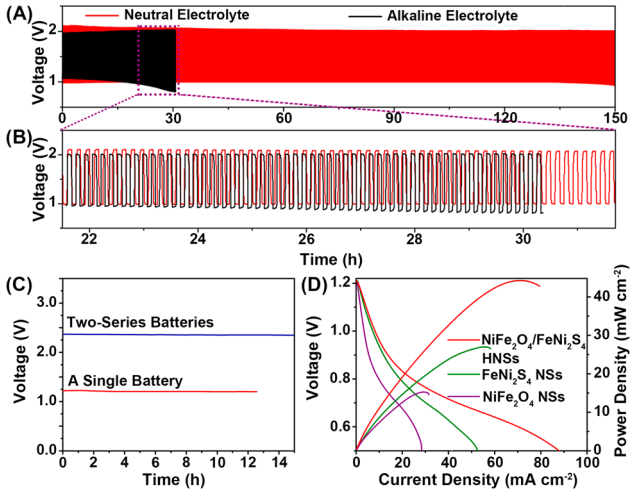

Figure 5. (A, B) Galvanostatic discharge−charge cycling curves (A) of the liquid RZABs at 0.5 mA cm^{-2} with $NiFe_2O_4/FeNi_2S_4$ HNSs as the catalyst in the different electrolytes and (B) the corresponding magnified view. (C) Open-circuit plots of a single and two-series neutral RZABs built by $NiFe_2O_4/FeNi_2S_4$ HNSs. (D) Polarization and power density curves of neutral RZABs with $NiFe_2O_4/FeNi_2S_4$ HNSs, $FeNi_2S_4$ NSs, and $NiFe_2O_4$ NSs as air-cathodes.

substantially improved in the more electrode-friendly neutral media. When 4.0 M NH_4Cl and 2.0 M KCl (pH = 7.0) is used as the electrolyte, the ZAB shows almost no decrease in round-trip efficiency (from 47.3% to 46.7%, only 0.6% decay) after 900 discharge/charge cycles, at a constant current density of 0.5 mA cm^{-2}. Even at a higher current density of 2 mA cm^{-2}, it still presents an appealing stability (Figure S18) and thus can be recognized as an efficient RZAB. We note that by using the neutral electrolyte, the as-described RZAB still maintains charge/discharge voltages (2.10/0.98 V) similar to the alkaline ZAB (1.97/1.08 V, Figure 5A and B), allowing it to be used as an environment-friendly energy device for equipment with a low current/power density requirement. Figure 5C illustrates that, at open circuit status, the RZAB can maintain a stable voltage for more than 12 h (1.22 V for single battery, 2.37 V for two-series batteries), indicating zinc corrosion is minimized in the neutral electrolyte. The polarization and power density curves of all the batteries are presented in Figure 5D, showing that the RZAB based on $NiFe_2O_4/FeNi_2S_4$ HNSs displays the highest power density of 44.4 mW cm^2, significantly superior to $FeNi_2S_4$ NSs (27.2 mW cm^2) or $NiFe_2O_4$ NSs (15.3 mW cm^2). This neutral RZAB with high discharging voltages and long-time stability is also the most robust one among RZABs reported to date.[9,10,S2]

4. CONCLUSION

In summary, well-defined $NiFe_2O_4/FeNi_2S_4$ HNSs are prepared via a facile wet-chemical sulfidation route and are demonstrated as an efficient and durable low-cost air-electrode catalyst for neutral RZABs. The as-synthesized $NiFe_2O_4/FeNi_2S_4$ HNSs feature a unique nanoparticle−overnanosheet architecture that exposes abundant oxide/sulfide interfaces, which lowers the oxygen adsorption energy and thus improves both OER and ORR kinetics. In 0.2 M PBS, the $NiFe_2O_4/FeNi_2S_4$ HNSs present much lower overpotentials for OER and ORR than $FeNiS_4$ and $NiFe_2O_4$. More importantly, the $NiFe_2O_4/FeNi_2S_4$ HNSs can be used to deliver the most robust RZAB with a neutral aqueous electrolyte reported to date, with a power density of 44.4 mW cm^{-2}, while maintaining a superior cycling stability (only 0.6% decay after 900 cycles at 0.5 mA cm^{-2}). This work provides a new strategy to improve the oxygen electrocatalysis for more efficient and environmentally friendly rechargeable metal−air batteries.

■ ASSOCIATED CONTENT

Supporting Information

The Supporting Information is available free of charge on the ACS Publications website at DOI: 10.1021/jacs.8b09805.

Tables S1−S7; Figures S1−S18 (PDF)

■ AUTHOR INFORMATION

Corresponding Authors

*xipx@lzu.edu.cn
*sz3t@virginia.edu

ORCID

Zhiyong Zhang: 0000-0001-7936-9510
Pinxian Xi: 0000-0001-5064-5622
Sen Zhang: 0000-0002-1716-3741

Author Contributions

#These authors contributed equally to this work.

Notes

The authors declare no competing financial interest.

■ ACKNOWLEDGMENTS

We acknowledge support from the National Natural Science Foundation of China (nos. 21571089, 51671003, 51571125), the Fundamental Research Funds for the Central Universities (lzujbky-2018-k08, lzujbky-2016-k02, lzujbky-2018-it40, and lzujbky-2017-it42), and U.S. National Science Foundation (DMR-1809700).

■ REFERENCES

(1) Larcher, D.; Tarascon, J. M. Towards Greener and More Sustainable Batteries for Electrical Energy Storage. *Nat. Chem.* **2015**, *7*, 19−29.

(2) Gao, M. R.; Xu, Y. F.; Jiang, J.; Yu, S. H. Nanostructured Metal Chalcogenides: Synthesis, Modification, and Applications in Energy Conversion and Storage Devices. *Chem. Soc. Rev.* **2013**, *42*, 2986−3017.

(3) Chen, L.-F.; Feng, Y.; Liang, H.-W.; Wu, Z.-Y.; Yu, S.-H. Macroscopic-Scale Three-Dimensional Carbon Nanofiber Architectures for Electrochemical Energy Storage Devices. *Adv. Energy Mater.* **2017**, *7*, 1700826.

(4) Meng, F.; Zhong, H.; Bao, D.; Yan, J.; Zhang, X. In Situ Coupling of Strung Co_4N and Intertwined N−C Fibers toward Free-Standing Bifunctional Cathode for Robust, Efficient, and Flexible Zn−Air Batteries. *J. Am. Chem. Soc.* **2016**, *138*, 10226−10231.

(5) Yi, J.; Ya-Ping, D.; Jing, F.; Un, L. D.; Ruilin, L.; Paul, C. Z.; Yangshuai, L.; Zhengyu, B.; Sooyeon, H.; Lin, Y.; Dong, S.; Weiguo, C.; Zhongwei, C. Interpenetrating Triphase Cobalt-Based Nanocomposites as Efficient Bifunctional Oxygen Electrocatalysts for Long-Lasting Rechargeable Zn−Air Batteries. *Adv. Energy Mater.* **2018**, *8*, 1702900.

(6) Liang, H.-W.; Wu, Z.-Y.; Chen, L.-F.; Li, C.; Yu, S.-H. Bacterial Cellulose Derived Nitrogen-Doped Carbon Nanofiber Aerogel: An Efficient Metal-Free Oxygen Reduction Electrocatalyst for Zinc-Air Battery. *Nano Energy* **2015**, *11*, 366−376.

(7) Li, Y.; Dai, H. Recent Advances in Zinc−Air Batteries. *Chem. Soc. Rev.* **2014**, *43*, 5257−5275.

DOI: 10.1021/jacs.8b09805
J. Am. Chem. Soc. 2018, 140, 17624−17631

(8) Li, Y.; Lu, J. Metal−Air Batteries: Will They Be the Future Electrochemical Energy Storage Device of Choice? *ACS Energy Lett.* **2017**, *2*, 1370−1377.
(9) Sumboja, A.; Ge, X.; Zheng, G.; Goh, F. W. T.; Hor, T. S. A.; Zong, Y.; Liu, Z. Durable Rechargeable Zinc−Air Batteries with Neutral Electrolyte and Manganese Oxide Catalyst. *J. Power Sources* **2016**, *332*, 330−336.
(10) Thomas Goh, F. W.; Liu, Z.; Hor, T. S. A.; Zhang, J.; Ge, X.; Zong, Y.; Yu, A.; Khoo, W. A Near-Neutral Chloride Electrolyte for Electrically Rechargeable Zinc-Air Batteries. *J. Electrochem. Soc.* **2014**, *161*, A2080−A2086.
(11) Simon, C.; Arnulf, L.; Birger, H. Rational Development of Neutral Aqueous Electrolytes for Zinc−Air Batteries. *ChemSusChem* **2017**, *10*, 4735−4747.
(12) Xu, K.; Cheng, H.; Liu, L.; Lv, H.; Wu, X.; Wu, C.; Xie, Y. Promoting Active Species Generation by Electrochemical Activation in Alkaline Media for Efficient Electrocatalytic Oxygen Evolution in Neutral Media. *Nano Lett.* **2017**, *17*, 578−583.
(13) Su, Y.; Zhu, Y.; Yang, X.; Shen, J.; Lu, J.; Zhang, X.; Chen, J.; Li, C. A Highly Efficient Catalyst toward Oxygen Reduction Reaction in Neutral Media for Microbial Fuel Cells. *Ind. Eng. Chem. Res.* **2013**, *52*, 6076−6082.
(14) Du, M.; Cui, L.; Cao, Y.; Bard, A. J. Mechanoelectrochemical Catalysis of the Effect of Elastic Strain on a Platinum Nanofilm for the ORR Exerted by a Shape Memory Alloy Substrate. *J. Am. Chem. Soc.* **2015**, *137*, 7397−7403.
(15) Reier, T.; Pawolek, Z.; Cherevko, S.; Bruns, M.; Jones, T.; Teschner, D.; Selve, S.; Bergmann, A.; Nong, H. N.; Schlögl, R.; Mayrhofer, K. J. J.; Strasser, P. Molecular Insight in Structure and Activity of Highly Efficient, Low-Ir Ir−Ni Oxide Catalysts for Electrochemical Water Splitting (OER). *J. Am. Chem. Soc.* **2015**, *137*, 13031−13040.
(16) Paoli, E. A.; Masini, F.; Frydendal, R.; Deiana, D.; Schlaup, C.; Malizia, M.; Hansen, T. W.; Horch, S.; Stephens, I. E. L.; Chorkendorff, I. Oxygen Evolution on Well-Characterized Mass-Selected Ru and RuO_2 Nanoparticles. *Chem. Sci.* **2015**, *6*, 190−196.
(17) Hunter, B. M.; Gray, H. B.; Müller, A. M. Earth-Abundant Heterogeneous Water Oxidation Catalysts. *Chem. Rev.* **2016**, *116*, 14120−14136.
(18) Xia, W.; Mahmood, A.; Liang, Z.; Zou, R.; Guo, S. Earth-Abundant Nanomaterials for Oxygen Reduction. *Angew. Chem., Int. Ed.* **2016**, *55*, 2650−2676.
(19) Shao, M.; Chang, Q.; Dodelet, J. P.; Chenitz, R. Recent Advances in Electrocatalysts for Oxygen Reduction Reaction. *Chem. Rev.* **2016**, *116*, 3594−3657.
(20) Wu, Z.-Y.; Xu, X.-X.; Hu, B.-C.; Liang, H.-W.; Lin, Y.; Chen, L.-F.; Yu, S.-H. Iron Carbide Nanoparticles Encapsulated in Mesoporous Fe-N-Doped Carbon Nanofibers for Efficient Electrocatalysis. *Angew. Chem., Int. Ed.* **2015**, *54*, 8179−8183.
(21) Fan, K.; Chen, H.; Ji, Y.; Huang, H.; Claesson, P. M.; Daniel, Q.; Philippe, B.; Rensmo, H.; Li, F.; Luo, Y.; Sun, L. Nickel−Vanadium Monolayer Double Hydroxide for Efficient Electrochemical Water Oxidation. *Nat. Commun.* **2016**, *7*, 11981.
(22) Xiaodong, Y.; Lihong, T.; Kexue, L.; Samuel, A.; Haifeng, Z.; James, M.; Lei, L.; Xiaobo, C. $FeNi_3/NiFeO_x$ Nanohybrids as Highly Efficient Bifunctional Electrocatalysts for Overall Water Splitting. *Adv. Mater. Interfaces* **2016**, *3*, 1600368.
(23) Gong, M.; Li, Y.; Wang, H.; Liang, Y.; Wu, J. Z.; Zhou, J.; Wang, J.; Regier, T.; Wei, F.; Dai, H. An Advanced Ni−Fe Layered Double Hydroxide Electrocatalyst for Water Oxidation. *J. Am. Chem. Soc.* **2013**, *135*, 8452−8455.
(24) Zhu, H.; Zhang, S.; Huang, Y.-X.; Wu, L.; Sun, S. Monodisperse $M_xFe_{3-x}O_4$ (M = Fe, Cu, Co, Mn) Nanoparticles and Their Electrocatalysis for Oxygen Reduction Reaction. *Nano Lett.* **2013**, *13*, 2947−2951.
(25) Zhiming, C.; Gengtao, F.; Yutao, L.; Goodenough, J. Ni_3FeN-Supported Fe_3Pt Intermetallic Nanoalloy as a High-Performance Bifunctional Catalyst for Metal−Air Batteries. *Angew. Chem., Int. Ed.* **2017**, *56*, 9901−9905.
(26) Liang, Y.; Li, Y.; Wang, H.; Zhou, J.; Wang, J.; Regier, T.; Dai, H. Co_3O_4 Nanocrystals on Graphene as a Synergistic Catalyst for Oxygen Reduction Reaction. *Nat. Mater.* **2011**, *10*, 780.
(27) Chunxian, G.; Yao, Z.; Jingrun, R.; Fangxi, X.; Mietek, J.; Shi-Zhang, Q. Engineering High-Energy Interfacial Structures for High-Performance Oxygen-Involving Electrocatalysis. *Angew. Chem., Int. Ed.* **2017**, *56*, 8539−8543.
(28) Ang, L.; Xiaoxia, C.; Zhiqi, H.; Chengcheng, L.; Yijia, W.; Lei, Z.; Tuo, W.; Jinlong, G. Thin Heterojunctions and Spatially Separated Cocatalysts To Simultaneously Reduce Bulk and Surface Recombination in Photocatalysts. *Angew. Chem., Int. Ed.* **2016**, *55*, 13734−13738.
(29) Zhao, S.; Jin, R.; Abroshan, H.; Zeng, C.; Zhang, H.; House, S. D.; Gottlieb, E.; Kim, H. J.; Yang, J. C.; Jin, R. Gold Nanoclusters Promote Electrocatalytic Water Oxidation at the Nanocluster/CoSe2 Interface. *J. Am. Chem. Soc.* **2017**, *139*, 1077−1080.
(30) Strickler, A. L.; Escudero-Escribano, M. a.; Jaramillo, T. F. Core−Shell Au@Metal-Oxide Nanoparticle Electrocatalysts for Enhanced Oxygen Evolution. *Nano Lett.* **2017**, *17*, 6040−6046.
(31) Yi, M. T.; Jingrun, R.; Sheng, D.; Mietek, J.; Zhang, Q. S. Phosphorus-Doped Graphitic Carbon Nitrides Grown In ;Situ on Carbon-Fiber Paper: Flexible and Reversible Oxygen Electrodes. *Angew. Chem., Int. Ed.* **2015**, *54*, 4646−4650.
(32) Ma, T. Y.; Dai, S.; Jaroniec, M.; Qiao, S. Z. Metal−Organic Framework Derived Hybrid Co_3O_4-Carbon Porous Nanowire Arrays as Reversible Oxygen Evolution Electrodes. *J. Am. Chem. Soc.* **2014**, *136*, 13925−13931.
(33) Qin, L.; Yaobing, W.; Liming, D.; Jiannian, Y. Scalable Fabrication of Nanoporous Carbon Fiber Films as Bifunctional Catalytic Electrodes for Flexible Zn-Air Batteries. *Adv. Mater.* **2016**, *28*, 3000−3006.
(34) Blöchl, P. E. Projector Augmented-Wave Method. *Phys. Rev. B: Condens. Matter Mater. Phys.* **1994**, *50*, 17953−17979.
(35) Perdew, J. P.; Burke, K.; Ernzerhof, M. Generalized Gradient Approximation Made Simple. *Phys. Rev. Lett.* **1996**, *77*, 3865−3868.
(36) Monkhorst, H. J.; Pack, J. D. Special Points for Brillouin-Zone Integrations. *Phys. Rev. B* **1976**, *13*, 5188−5192.
(37) Xu, Z.; Yipu, L.; Guo-Dong, L.; Yuanyuan, W.; Da-Peng, L.; Wang, L.; Hai-Wen, L.; Dejun, W.; Yu, Z.; Xiaoxin, Z. Ultrafast Formation of Amorphous Bimetallic Hydroxide Films on 3D Conductive Sulfide Nanoarrays for Large-Current-Density Oxygen Evolution Electrocatalysis. *Adv. Mater.* **2017**, *29*, 1700404.
(38) Long, X.; Li, G.; Wang, Z.; Zhu, H.; Zhang, T.; Xiao, S.; Guo, W.; Yang, S. Metallic Iron−Nickel Sulfide Ultrathin Nanosheets As a Highly Active Electrocatalyst for Hydrogen Evolution Reaction in Acidic Media. *J. Am. Chem. Soc.* **2015**, *137*, 11900−11903.
(39) Zhenlu, Z.; Haoxi, W.; Haili, H.; Xiaolong, X.; Yongdong, J. A High-Performance Binary Ni−Co Hydroxide-based Water Oxidation Electrode with Three-Dimensional Coaxial Nanotube Array Structure. *Adv. Funct. Mater.* **2014**, *24*, 4698−4705.
(40) Jian, Z.; Tao, W.; Darius, P.; Bernd, R.; Renhao, D.; Shaohua, L.; Xiaodong, Z.; Xinliang, F. Interface Engineering of MoS_2/Ni_3S_2 Heterostructures for Highly Enhanced Electrochemical Overall-Water-Splitting Activity. *Angew. Chem., Int. Ed.* **2016**, *55*, 6702−6707.
(41) Nørskov, J. K.; Rossmeisl, J.; Logadottir, A.; Lindqvist, L.; Kitchin, J. R.; Bligaard, T.; Jónsson, H. Origin of the Overpotential for Oxygen Reduction at a Fuel-Cell Cathode. *J. Phys. Chem. B* **2004**, *108*, 17886−17892.
(42) Rossmeisl, J.; Qu, Z. W.; Zhu, H.; Kroes, G. J.; Nørskov, J. K. Electrolysis of Water on Oxide Surfaces. *J. Electroanal. Chem.* **2007**, *607*, 83−89.
(43) Busch, M.; Halck, N. B.; Kramm, U. I.; Siahrostami, S.; Krtil, P.; Rossmeisl, J. Beyond the Top of the Volcano? − A Unified Approach to Electrocatalytic Oxygen Reduction and Oxygen Evolution. *Nano Energy* **2016**, *29*, 126−135.
(44) Koper, M. T. M. Thermodynamic Theory of Multi-Electron Transfer Reactions: Implications for Electrocatalysis. *J. Electroanal. Chem.* **2011**, *660*, 254−260.

DOI: 10.1021/jacs.8b09805
J. Am. Chem. Soc. 2018, 140, 17624−17631

(45) Lee, Y.-L.; Kleis, J.; Rossmeisl, J.; Shao-Horn, Y.; Morgan, D. Prediction of Solid Oxide Fuel Cell Cathode Activity with First-Principles Descriptors. *Energy Environ. Sci.* **2011**, *4*, 3966−3970.
(46) Man, I.; Su, H.; Calle-Vallejo, H.; Hansen, H.; Martinez, J.; Inoglu, N.; Kitchin, J.; Jaramillo, T.; Norskov, J.; Rossmeisl, J. Universality in Oxygen Evolution Electrocatalysis on Oxide Surfaces. *ChemCatChem* **2011**, *3*, 1159−1165.
(47) Calle-Vallejo, F.; Díaz-Morales, O. A.; Kolb, M. J.; Koper, M. T. M. Why Is Bulk Thermochemistry a Good Descriptor for the Electrocatalytic Activity of Transition Metal Oxides? *ACS Catal.* **2015**, *5*, 869−873.
(48) Wang, Y.; Cheng, H.-P. Oxygen Reduction Activity on Perovskite Oxide Surfaces: A Comparative First-Principles Study of $LaMnO_3$, $LaFeO_3$, and $LaCrO_3$. *J. Phys. Chem. C* **2013**, *117*, 2106−2112.
(49) Nakagawa, T.; Bjorge, N. S.; Murray, R. W. Electrogenerated IrO_x Nanoparticles as Dissolved Redox Catalysts for Water Oxidation. *J. Am. Chem. Soc.* **2009**, *131*, 15578−15579.
(50) Wang, Z.; Xiao, S.; Zhu, Z.; Long, X.; Zheng, X.; Lu, X.; Yang, S. Cobalt-Embedded Nitrogen Doped Carbon Nanotubes: A Bifunctional Catalyst for Oxygen Electrode Reactions in a Wide pH Range. *ACS Appl. Mater. Interfaces* **2015**, *7*, 4048−4055.
(51) Xien, L.; Minjoon, P.; Gyu, K. M.; Shiva, G.; Gang, W.; Jaephil, C. Integrating NiCo Alloys with Their Oxides as Efficient Bifunctional Cathode Catalysts for Rechargeable Zinc−Air Batteries. *Angew. Chem., Int. Ed.* **2015**, *54*, 9654−9658.
(52) Deng, Z.; Yi, Q.; Li, G.; Chen, Y.; Yang, X.; Nie, H., NiCo-doped C-N Nano-Composites for Cathodic Catalysts of Zn-Air Batteries in Neutral Media. *Electrochim. Acta* **2018**, *279*, 1.

DOI: 10.1021/jacs.8b09805
J. Am. Chem. Soc. 2018, 140, 17624−17631